

RESEARCH ARTICLE

10.1002/2017JB014624

Special Section:

Gas Hydrate in Porous Media: Linking Laboratory and Field Scale Phenomena

Key Points:

- We used different strategies to accelerate the supply of guest molecules to the hydrate formation front in fine-grained sediments
- Hydrate formation in fine-grained sediments is inherently displacive and segregated
- Exo-pore hydrate growth is striped and porous and prolongs fast hydrate growth

Correspondence to:

L. Lei,
liang.lei@netl.doe.gov

Citation:

Lei, L., & Santamarina, J. C. (2018). Laboratory strategies for hydrate formation in fine-grained sediments. *Journal of Geophysical Research: Solid Earth*, 123. <https://doi.org/10.1002/2017JB014624>

Received 28 JUN 2017

Accepted 27 MAR 2018

Accepted article online 2 APR 2018

Laboratory Strategies for Hydrate Formation in Fine-Grained Sediments

L. Lei¹  and J. C. Santamarina²¹National Energy Technology Laboratory, U.S. Department of Energy, Morgantown, WV, USA, ²Earth Science and Engineering, KAUST, Thuwal, Saudi Arabia

Abstract Fine-grained sediments limit hydrate nucleation, shift the phase boundary, and hinder gas supply. Laboratory experiments in this study explore different strategies to overcome these challenges, including the use of a more soluble guest molecule rather than methane, grain-scale gas-storage within porous diatoms, ice-to-hydrate transformation to grow lenses at predefined locations, forced gas injection into water saturated sediments, and long-term guest molecule transport. Tomographic images and thermal and pressure data provide rich information on hydrate formation and morphology. Results show that hydrate formation is inherently displacive in fine-grained sediments; lenses are thicker and closer to each other in compressible, high specific surface area sediments subjected to low effective stress. Temperature and pressure trajectories follow a shifted phase boundary that is consistent with capillary effects. Exo-pore growth results in freshly formed hydrate with a striped and porous structure; this open structure becomes an effective pathway for gas transport to the growing hydrate front. Ice-to-hydrate transformation goes through a liquid stage at premelt temperatures; then, capillarity and cryogenic suction compete, and some water becomes imbibed into the sediment faster than hydrate reformation. The geometry of hydrate lenses and the internal hydrate structure continue evolving long after the exothermal response to hydrate formation has completely decayed. Multiple time-dependent processes occur during hydrate formation, including gas, water and heat transport, sediment compressibility, reaction rate, and the stochastic nucleation process. Hydrate formation strategies conceived for this study highlight the inherent difficulties in emulating hydrate formation in fine-grained sediments within the relatively short time scale available for laboratory experiments.

1. Introduction

The accumulation of methane in hydrate-bearing sediments exceeds 20,000 trillion m³ (Boswell, 2009). Hydrate-bearing coarse-grained sediments are preferred for potential gas production due to their relatively high saturation, high permeability, nondisplacive pore habit, and low volume contraction upon dissociation (Moridis et al., 2009; Yamamoto & Dallimore, 2008). Consequently, laboratory studies have focused on hydrate formation in coarse-grained sediments and have used various formation strategies to overcome the low methane solubility in water: advection of gas saturated water, partial water saturated sediments pressurized with gas, pulverized-ice seeding, and pulverized-hydrate premixing with cooled sediments (Ebinuma et al., 2005; Katsuki et al., 2006; Waite et al., 2009; Zhong & Rogers, 2000). Alternatively, some studies have used more soluble guest molecules, from stoichiometric tetrahydrofuran (THF) solutions (Lee et al., 2007) and cyclopentane (Aman et al., 2011, 2013), to carbon dioxide (Katsuki et al., 2006; Tohidi et al., 2001; Zatsepina & Buffett, 2001).

The accumulation of methane hydrates in fine-grained sediments exceeds the accumulation in sands by an order of magnitude (Boswell & Collett, 2011). Yet there are no published studies of hydrate formation in fine-grained sediments that utilize gas as guest molecules; consequently, hydrate-bearing fine-grained sediments remain less understood and characterized than sandy reservoirs.

The small pore size found in fine-grained sediments and the associated capillarity and water-mineral interactions hinder nucleation and shift the gas hydrate phase boundary to higher pressures and lower temperatures (Handa & Stupin, 1992; Park et al., 2016; Seshadri et al., 2001; Uchida et al., 2001). Hydrate growth is displacive in fine-grained sediments, and the hydrate mass is found in segregated nodules, lenses, and veins (Clennell et al., 1999; Dai et al., 2012), as confirmed by borehole electrical resistivity measurements (Cook et al., 2008), photographs of recovered cores from a variety of drill sites, and X-ray CT images of pressure

Table 1
Sediment Properties

Soil type	Minerology	Mean particle size D_{50} [μm]	Specific surface S_s [m^2/g]	Liquid limit LL [%]
Silica flour	SiO_2	20	0.5	31
Kaolinite	$\text{Al}_2\text{Si}_2\text{O}_5(\text{OH})_4^{\text{a}}$	0.4^{b}	34	67
Diatom	92% SiO_2^{c}	10^{c}	89	121
Bentonite	$\text{Al}_2\text{H}_2\text{Na}_2\text{O}_{13}\text{Si}_4^{\text{d}}$	0.07^{e}	565	276
Hydrophobic silica	SiO_2 coated with chlorosilanes	$\approx 0.04^{\text{f}}$	32^{f}	Does not apply

^aReade Advanced Materials. ^bPalomino and Santamarina (2005). ^cPERMA-GUARD. ^dSodium bentonite. ^ePlaschke et al. (2001). ^fEstimated from SEM images.

cores (Ghosh et al., 2010; Lee et al., 2013; Rees et al., 2011). Lens extension/persistence and the maximum nodule size remain unknown as observations are limited by core-size. Yet common features have emerged from images reported in the last decade (Collett et al., 2008; Lee et al., 2013; Yamamoto et al., 2012; Yun et al., 2011): (1) Individual lenses have jagged sediment-hydrate interfaces; (2) lenses are often in groups, mostly parallel to each other, but with frequent intersections at small angles; (3) lens-groups intersect at large angles; (4) lens thickness ranges from ~ 1 to 100 mm, and lens spacing from ~ 10 mm to 1 m; and (5) nodules recovered inside cores are small (50-mm core diameter) and have smooth, curved surfaces.

Fine-grained sediments have inherently low permeability, which hinders gas transport to the gas-limited hydrate formation front. This study explores various methods to form hydrates in fine-grained sediments within the relatively short laboratory time scale. The experimental design, formation strategies, and salient observations are described here; for additional details, see Lei (2017).

2. Experimental Study: Devices and Materials

2.1. Sediments and Fluids

The tests involved six different sediments specifically selected to emulate various natural formations and range from silts to high plasticity clays and diatoms that are internally porous. Table 1 summarizes their key index properties. The fluids are deionized water, CO_2 gas (99.99% purity), and a stoichiometric THF solution.

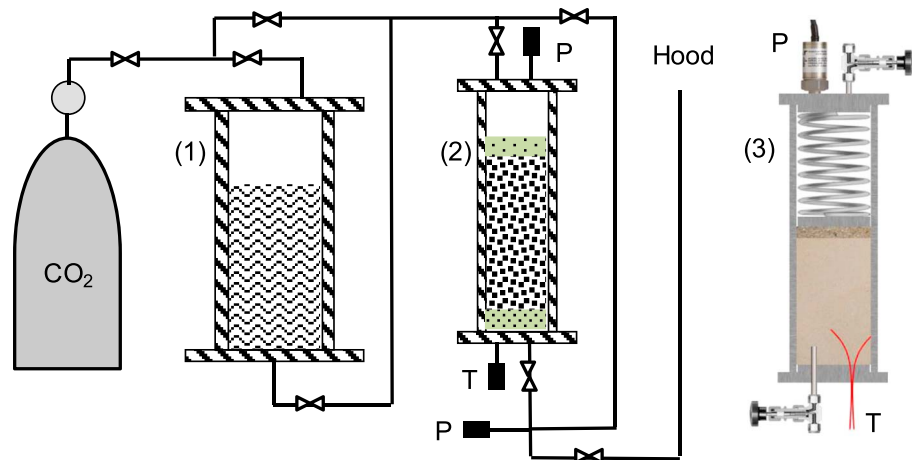
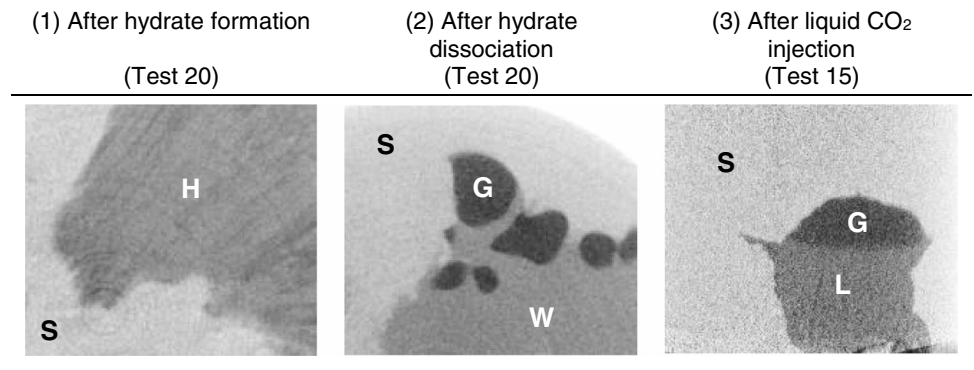


Figure 1. Reactor and pressure-temperature control system. The auxiliary chamber (1) facilitates gas and water control. The X-ray transparent reactor (2) includes an internal preloaded spring to apply a nominal effective stress (3). Instrumentation includes pressure transducers (P) and thermocouples (T).



Labels: S=Sediment, H=Hydrate, G=Gas, W=Water, L=Liquid CO₂

Figure 2. Feature identification—examples. (1) Striped and porous hydrate. (2) Segregated water after hydrate dissociation. (3) Gravity segregated gas and liquid CO₂.

2.2. Vessel, Pressure Control, and Instrumentation

Figure 1 presents a pressure-and-flow control system designed to inject gas and/or gas-saturated water to both the top and bottom of three specimen chambers which are connected in parallel. The thin-walled (3.5 mm) aluminum chambers ($\varnothing = 40$ mm, $H = 140$ mm) can sustain fluid pressures up to 30 MPa. The segregated hydrate morphology in fine-grained sediments implies hydrate growth against the effective confining stress; thus, these chambers house a precompressed spring to maintain a nominal effective vertical stress on the specimen under zero-lateral strain conditions, that is, stress anisotropy $k_{\sigma} \sim 0.6$ – 0.7 (Figure 1; see Table 1 for stress history). X-ray projections show homogeneous specimens in all cases. Thermocouples and pressure transducers monitor the temperature and fluid pressure inside each chamber.

2.3. X-ray Tomography

We use X-ray computed tomography to observe the hydrate formation process. Key considerations include the balance between X-ray source strength, material X-ray transparency, ease of operation, and specimen size effect. The micro focus CT scanner built for this study has a 130-kV source and a $1,024 \times 1,024$ element flat panel detector. The attainable imaging resolution for the 40-mm chamber is a 40- μm voxel size.

The typical scan time exceeds 30 min; we insulate the chamber with X-ray transparent foam to reduce heat absorption from the environment. An accurate base-mount attaches the aluminum chamber to the rotary stage and allows for successive scans at the same position to facilitate the comparison of tomograms gathered at different stages of the imposed P-T history.

The voxel intensity in 3-D X-ray tomograms corresponds to the local attenuation coefficient. There are six different materials involved in these tests: the aluminum chamber, the water saturated sediment, segregated water, segregated hydrate, liquid CO₂, and gases. Any air dissolved in the water is excluded from hydrate formation and forms bubbles. The histograms of voxel intensities for hydrate, water, and liquid CO₂ overlap quite extensively, and it is difficult to differentiate between these materials at small scales. Previous CT studies have used xenon hydrate or a potassium iodide solution to separate the hydrate phase from the pore fluid (Jin et al., 2008; Ta et al., 2015). However, the segregated hydrate mass is readily identified in this study, by taking into consideration the following process-dependent observations (Figures 2 and 7): (1) evolution of tomographic images along with measured P-T conditions relative to phase stability boundaries; (2) water is either within the sediment pores and is imaged as an average sediment absorption or it reacts to form the hydrate mass; (3) water segregates after hydrate dissociation as the sediment skeleton compacts due to cryogenic suction; (4) hydrate can resist shear and adopt complex geometries, while immiscible fluids interact through curved Laplacian interfaces; (5) gravity segregates liquid CO₂ and water from gas; and (6) features thicker than ~ 2 pixels along the sediment-gas interface with an attenuation similar to hydrate are assumed to be hydrate shells. Most lens-like structures imaged/identified in this study are hydrate-filled.

Table 2
List of Experiments Conducted as Part of This Study

Test no.	Sediment type	Related figures	Liquid content ^a	Hydrate morphology	Notes
THF hydrate experiments					
1	Silica flour	6	40%	Pore-filling	THF/water molar ratio = 1/17. Supercooling to 2 °C before hydrate formation
2	Diatom	6	150%	Thin lenses	
3	Diatom (slow)	6	120%	Lenses	
4	Kaolinite	6	60%	Lenses	
5	Bentonite	6	300%	Lenses and blocks	
Particle inner pore space utilization (CO ₂ hydrate)					
6	Diatom	–	0% ⇒ 40%	Small crystals	Water injection into dry diatom specimen: #6&8 inside and #7 outside hydrate stability field
7	Diatom	–	0% ⇒ 30%	Hydrate flower	
8	Diatom	–	0% ⇒ 40%	Small crystals	
Ice-to-hydrate transformation (CO ₂ hydrate)					
9	Kaolinite	–	–	Porous lens	Ice lens in groove-unsaturated kaolinite Small sample with $D = 6$ mm, $L = 20$ mm
10	Kaolinite	–	60%	Shell	
11	Kaolinite	3	55%	Porous block	Unsaturated
12	Kaolinite	7	–	Porous lens	Dry kaolinite with embedded ice lens
13	Hydrophobic silica	–	–	Porous lens	Hydrophobic silica with large (#13) and small (#14) embedded ice lens
14	Hydrophobic silica	7	–	Lenses	
Forced gas injection (CO ₂ hydrate)					
15	Diatom	4	40%	Porous lens	1. Consolidation pressure: 50 kPa 2. Gas injection from bottom
16	Diatom	–	40%	Porous lens	
17	Layered specimen ^b	–	48%	Porous lens	Slurry-gas injection from bottom
18	Layered specimen ^c	–	48%	Porous lens	
19	Kaolinite	5	150%	Lens, shell	
20	Kaolinite	–	150%	Lens	
Long-term diffusion (CO ₂ hydrate)					
21	Bentonite	–	2000%	Stripped (hair)	Temperature depression after long-time CO ₂ diffusion
22	Bentonite	–	300%	Stripped and lens	

^aMass ratio between saturating liquid and dry sediment. ^bKaolinite, sand, and kaolinite. ^cSand on top of kaolinite.

3. Laboratory Study: Hydrate Formation Strategies

We designed different experimental strategies to overcome some of the inherent limitations with gas hydrate formation in fine-grained sediments discussed above and to explore underlying processes. Table 2 describes the 22 experiments conducted in this study. Figure 3 presents selected P-T trajectories (a detailed analysis of P-T responses is presented in the following section).

3.1. Strategy Based on THF Hydrate

Tetrahydrofuran is fully miscible with water. Therefore, hydrate formation can proceed without diffusion or advection limitations. This allows for relatively fast hydrate growth after nucleation, which is convenient for short-term laboratory studies. In nature, fast hydrate growth takes place immediately after hydrate nucleation because the methane solubility in water decreases as soon as the hydrate phase appears, and the pore fluid effectively becomes a supersaturated solution (Jang & Santamarina, 2016). THF hydrate conveniently forms at ~4 °C under atmospheric pressure, so no pressure vessel is needed; this facilitates heat flux control. We tested THF hydrate formation in the four selected sediments (tests 1 to 5, Table 2, at ~2 °C). The initial mass ratio between stoichiometric THF solution and dry sediment is slightly above the liquid limit in all tests (Table 1). Similarities and differences between CH₄ and THF hydrates are reviewed in Lee et al. (2007), while properties of THF hydrate bearing sediments are described by Yun et al. (2007).

3.2. Strategy Based on Diatoms

This series of experiments explores the storage of high-pressure CO₂ gas in the intraparticle space of dry diatoms (tests 6–8). After gas compression, we filled the specimen with water and allowed hydrate to form by consuming the readily available gas within diatoms, next to each sediment pore. Consequently, hydrate formation is not limited by the long diffusion time required for the transport of guest molecules from the

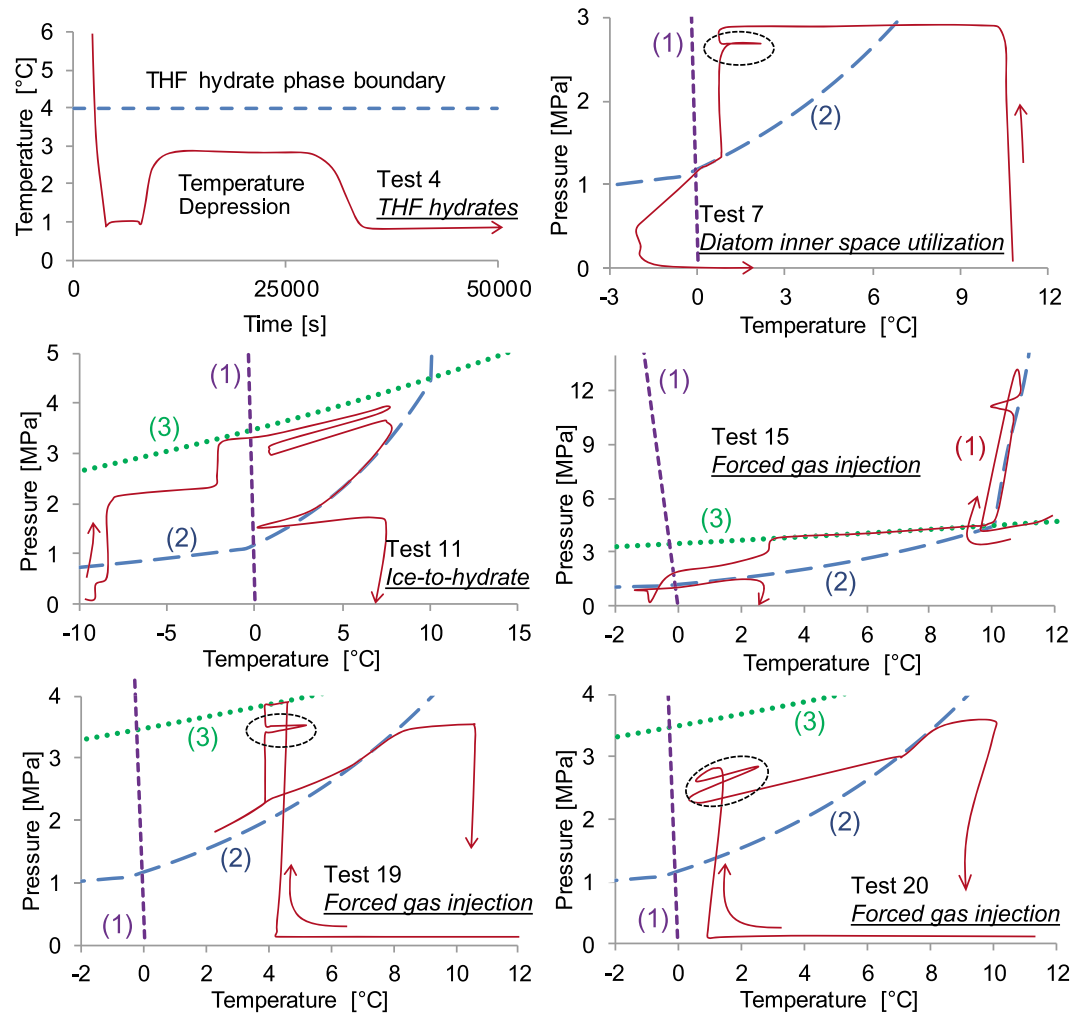


Figure 3. Typical P-T trajectories (red lines) for various tests (test numbers: refer to Table 2 for details). Phase boundary shown for (1) ice-water, (2) CO₂ hydrate, and (3) gas-liquid CO₂. Exothermic thermal spikes are readily seen in P-T trajectories for tests 4, 7, 19, and 20.

specimen boundary. This strategy is agreeable with the presence of hydrates in fine-grained diatomaceous marine sediments (Clennell et al., 1999; Yun et al., 2011).

3.3. Strategy Based on Ice-to-Hydrate Transformation

Ice coexists with CH₄ hydrate under permafrost conditions, where ice-to-hydrate transformation takes place in response to P-T conditions associated with climate change and burial (Dai et al., 2011). Ice-to-hydrate transformation has been used to facilitate gas hydrate formation by reducing the nucleation barrier; we adapted this strategy to grow hydrate lenses at predefined locations within fine-grained sediments. We start with either (1) frozen unsaturated sediments (saturation below the level required for free gas percolation) or (2) with premade ice lenses buried in cold dry specimens to ensure a percolating gas phase across the specimen. Then we increase the CO₂ gas pressure into the hydrate stability field at -15°C , 2 MPa. Finally, we favor ice-to-hydrate transformation by gradually increasing the temperature toward the ice melting point ($\Delta T = +0.5^{\circ}\text{C}$ steps every 2 hr) under constant gas pressure, inside the hydrate stability field (tests 9 to 14, Table 2).

3.4. Strategy Based on Forced Gas Injection

Methane seeps imply the presence of free gas pathways within the sediment, either in the form of gas-filled pipes in sands or gas-driven fractures in silty and clayey sediments (Chen et al., 2016; Gardner et al., 2009; Graves et al., 2017; Schwalenberg et al., 2017). Hydrate formation along and around these conduits

depends on the rate of gas transfer and water supply to the hydrate formation front. We inject CO₂ into water-saturated sediments to cause gas-driven fractures (see tests 15 and 19 in Figure 3 for typical P-T trajectories—tests 15 to 18 are under 50-kPa vertical effective stress within the spring loaded cell in Figure 1b). We also inject gas into slurries to create consecutive bubbles similar to near-surface seafloor conditions (tests 19 and 20—P-T trajectories in Figure 3).

3.5. Strategy Based on Long Duration Diffusion of Reactants

In natural systems, diffusion is the prevailing gas transport process in saturated fine-grained sediments away from active gas conduits and coarse-grained layers. Water-saturated specimens in tests 21 and 22 are surrounded by CO₂ at 3 MPa and 12 °C for a maturation period of 20 and 10 days, respectively. Then, we lower the temperature in the hydrate stability field to 2 °C. The anticipated CO₂ diffusion length during the maturation period $L = \sqrt{D \cdot t}$ is in the order of several centimeters in both tests (note: The diffusion coefficient is lower in bulk water because of tortuosity and physiochemical interactions with mineral surfaces; Clennell et al., 2000); the gravimetric water content in tests 21 and 22 exceeds ~90%, so we adopt the value of diffusion for bulk water as a first-order approximation).

4. Results and Observations

The different strategies outlined above were conceived to facilitate the supply of guest molecules to the hydrate formation front, to overcome the nucleation barrier, and to explore long-term diffusion-controlled gas hydrate formation in sediments. The most striking observation from this study is the inherent difficulty in emulating hydrate formation in fine-grained sediments within the relatively short time scales in laboratory settings. However, all tests contributed relevant information and provided new insights. This section reports common features and salient observations gathered in this study.

4.1. Pressure and Temperature Effects

4.1.1. P-T Trajectories: Observations

Figure 3 presents a selection of pressure-temperature trajectories recorded in the study. Temperature-time signatures all exhibit a common sequence of characteristic features: induction time, supercooling, or overpressuring prior to phase transformation, exothermic/endothemic transients during phase transformation (Figure 3: test 4. See Dai et al., 2014). P-T trajectories follow phase boundaries when phase transitions are involved, including water-ice, liquid-gas CO₂, and the hydrate phase boundary (Figure 3: all cases). P-T trajectories frequently diverge from the known phase boundaries (Figure 3: test 11 for the L-G transition). While physicochemical effects may be involved, apparent phase boundary shifts often reflect the spatial mismatch between the position of the thermocouples and the location where transformations take place. To avoid biases, thermocouples (accuracy: ±0.1 K, response time: <1 s in sediment, <5 s in gas) and pressure transducers (accuracy: ±0.25% BSL, response time: <1 ms) are carefully calibrated before each test.

4.1.2. Thermal Spikes

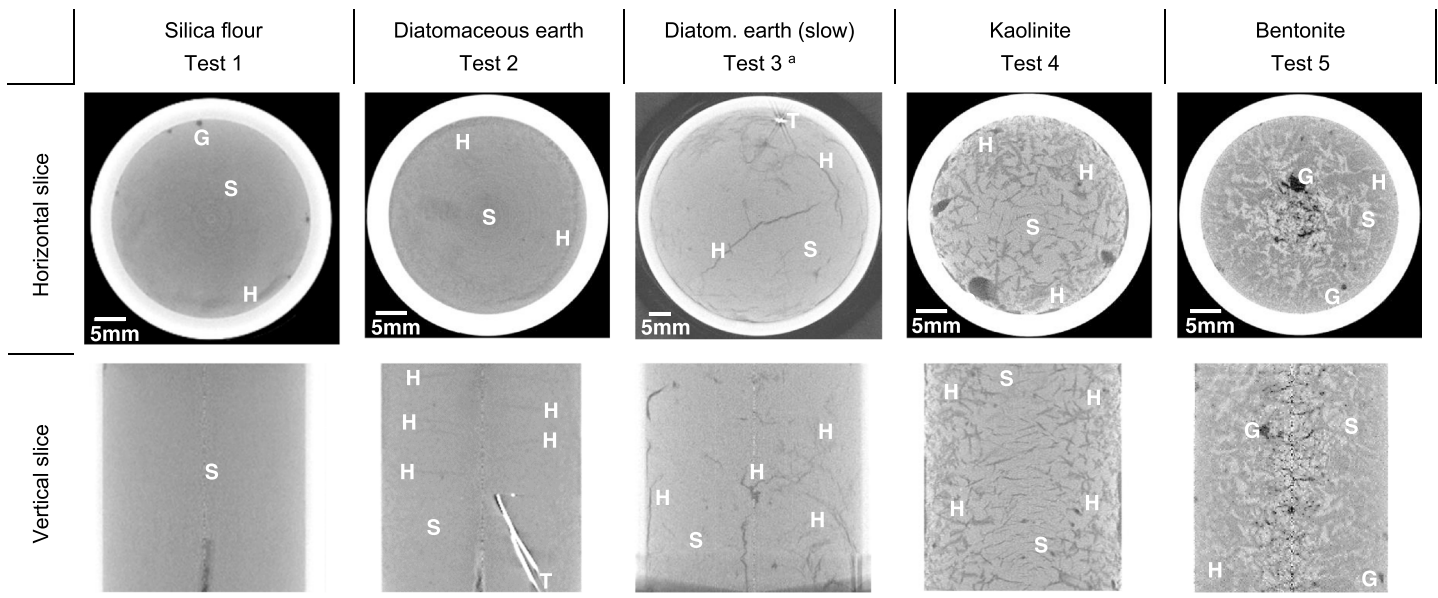
Hydrate formation is exothermic. Thermal spikes are readily seen in the P-T trajectories (Figure 3: tests 7, 19, and 21). The thermal spike from THF hydrate formation lasts about 30 min when hydrate formed in silica flour but continues for several hours when hydrate formed in kaolinite and bentonite (Figure 3: test 4). The duration and intensity of thermal spikes relate to the rate of formation, the rate of heat transfer owing to thermal conduction, and the total amount of hydrate that formed. Thermal spikes are lower and shorter in CO₂ hydrate formation in comparison to stoichiometric THF hydrate formation tests because of slow CO₂ supply.

4.1.3. Temperature Depression

The temperature depression during phase transformation is more pronounced in smaller pores, that is, finer grained sediments and more pronounced effects of water-mineral interactions. Thus, high-curvature hydrates form last but dissociate first (Anderson et al., 2003; Rempel, 2011a). The P-T trajectory for test 19 in Figure 3 displays the typical response when the transformation is affected by pore confinement effects: The P-T trajectory follows the shifted phase boundary as the temperature decreases toward 2 °C. During thermal stimulation, the P-T trajectory follows the same shifted boundary first and gradually converges toward the bulk hydrate phase boundary as the temperature increases to >6 °C.

4.1.4. Premelting in Ice-to-Hydrate Transformation

The ice-to-hydrate transformation occurs at temperatures 1.5 to 1.7 °C lower than the ice melting point (tests 10 to 14). Two concurrent effects explain this observation:



Labels: S=Sediment, G=Gas, H=Hydrate, T=Thermocouple

Figure 4. Tetrahydrofuran (THF) hydrate morphology in different sediments. All specimens are housed inside the aluminum chambers and cooled in a water bath, except for the slow-cooling test 3 where the diatomaceous earth specimen is housed in a plastic tube and cooled in an air-bath. The saturating fluid is stoichiometric THF solution in all tests. Various hydrate morphologies are observed. Test 1: disseminated hydrate with minor segregation near the upper free boundary. Test 2: peripheral hydrate ring and parallel horizontal lenses toward the center of the specimen. Test 3: peripheral hydrate ring and large vertical lens across the center. Test 4: multiple peripheral lenses with fewer lenses toward the center. Test 5: massive hydrate surrounds clay inclusions (brighter features), and excluded air remains at the center.

1. The latent heat for CO_2 hydrate formation-dissociation is ~ 60 kJ/mol (Anderson, 2003), while the latent heat for water-ice transformation is 6.05 kJ/mol; therefore, the ice-to- CO_2 -hydrate transformation is an exothermic process (~ 25 kJ per mole of hydrate).
2. Premelting commences at the ice crystal surface when $T = -33$ °C; in fact, the ice crystal surface structure does not fully resemble the interior structure even at extremely low temperatures (Li & Somorjai, 2007).

Therefore, the transformation from ice-to-hydrate occurs on the premelted ice surface, and the generated heat melts more ice to release free water for further hydrate formation. This positive feedback loop sustains ice-to-hydrate transformation before the anticipated -0.22 °C for ice-water melting under 3-MPa pressure (see a parallel analysis for CH_4 - CO_2 replacement in Jung et al., 2010).

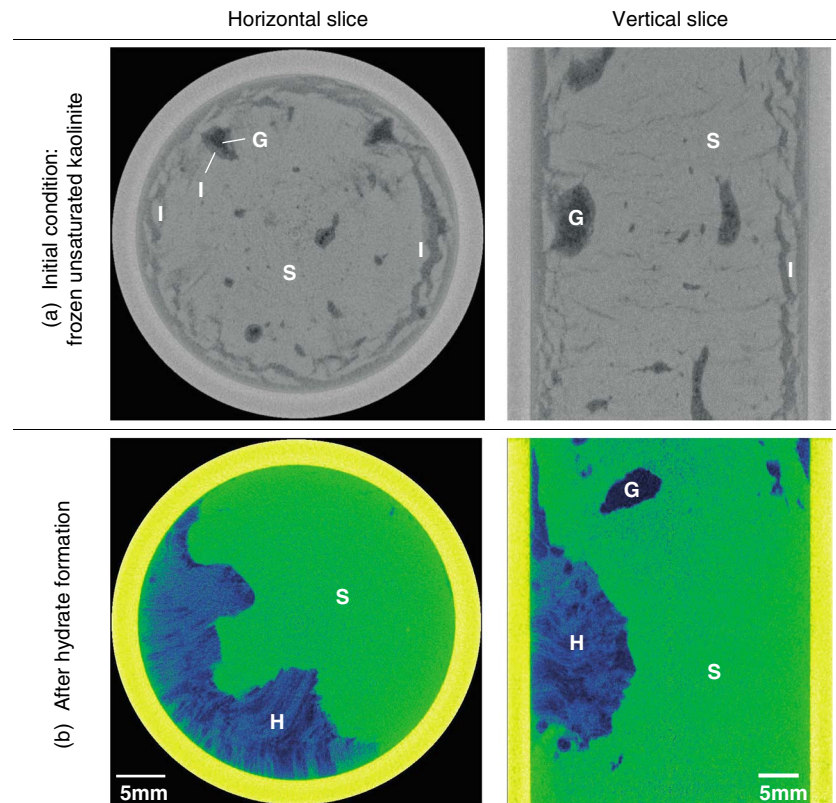
4.2. Hydrate Morphology: Characteristics

4.2.1. Small Hydrate Crystals in Diatomaceous Earth

Temperature and pressure trajectories and related mass analyses indicate that hydrate formed in all diatomaceous earth specimens (tests 6 to 8). Yet there are no clear signs of segregated CO_2 hydrate in any of the CT images. These results suggest that small hydrate crystals do form in pores but do not merge into the large segregated hydrate mass that could be distinguished in CT images with 40- μm resolution (note: intrapores are quite large, and amorphous silica has relatively weak interaction with water; hence, hydrate may crystallize within diatoms). Long time scales in nature may allow for Ostwald-ripening resulting in the segregated hydrate structure observed in the diatomaceous sediments found in the Ulleung Basin (Yun et al., 2011).

4.2.2. THF Hydrate Morphology

Guest molecules are readily available in the stoichiometric THF solution. Consequently, thermal boundary conditions, sediment properties, and the evolving stress field control the morphology of the hydrate mass as it forms and segregates, similar to ice lens formation (Azmatch et al., 2012; Miller, 1972; O'Neill & Miller, 1985; Rempel, 2011b; Taber, 1930; Viggiani et al., 2015). Displacive hydrate formation pulls water from the



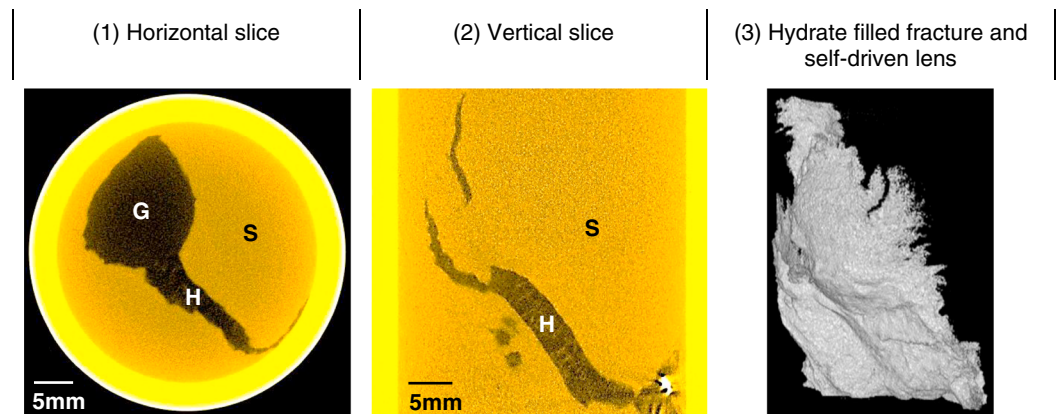
Labels: S=Sediment, I=Ice, G=Gas, H=Porous Hydrate

Figure 5. Ice-to-hydrate transformation: unsaturated frozen kaolinite (test 11 in Table 2). The CO₂ hydrate mass is shown in blue. Ice formed and grew near the periphery and compacted the clay mass, and ice lenses are less pronounced toward the center. On the contrary, the hydrate mass is porous with a marked stripe pattern, and it concentrates on one side (i.e., extensive water migration and redistribution during hydrate formation). Note: An ice shell surrounds large air bubbles originally present in the specimen.

compressible sediment, that is, cryogenic suction; the denser sediment that surrounds the segregated hydrate mass exhibits a higher CT number or X-ray attenuation (Figure 4). Indeed, coarser and stiffer sediments develop fewer hydrate lenses as the particle-displacive trend diminishes (silt and diatoms; Figure 4). In kaolinite and bentonite specimens, closely spaced lenses grow toward the center first; the remaining central region is more compact and develops more sporadic lenses. Finally, note that slow heat dissipation favors the formation of larger and more localized hydrate lenses (Figure 4: Compare test 2 cooled in a water bath versus test 3 cooled in air). While the stoichiometric THF solution is used in both tests, a liquid phase remains in the small pores of fine-grained sediments after hydrate lens formation (tests 4 and 5). All THF could form pore-filling hydrate in test 1 (we do not have direct evidence). Early tests with water-saturated fine-grained sediments under similar boundary conditions produced ice lens morphologies similar but not identical to segregated THF hydrate morphologies. We infer that differences in supercooling and in the initial sediment fabrics that formed in water as compared to the THF solution affect the evolution of lenses.

4.2.3. CO₂ Hydrate Structure: Porosity

In addition to variables explored with THF hydrate, gas transport plays a critical role on the evolving hydrate morphology when hydrate formation is gas limited. Some tomograms show a striped-fibrous hydrate structure (Figure 5) that resembles images reported for hydrate formation in pipe clogging studies (Makogon, 1997) and hair-ice (Hofmann et al., 2015). However, the most salient characteristic observed in young hydrate lenses is their porous structure made of separate crystals/fibers (Figure 2: test 20; Figure 6: test 15 and also observed in tests 6, 9, 11, 12, and 16–22). Striped and porous hydrates are forms of exo-pore growth where hydrates grow outside the pores at a free surface or into a preexisting gas-driven opening.



Labels: S= Sediment, G=Gas, H=Porous Hydrate

Figure 6. Gas-driven fracture in a water saturated kaolinite specimen (test 15 in Table 2). (1) Horizontal slice and (2) vertical section. Porous CO₂ hydrate forms in the gas-driven fracture and continues developing long after the initial gas injection and breakthrough. (3) 3-D hydrate mass that formed inside the gas-driven fracture (extracted from the 3-D tomographic image).

4.2.4. CO₂ Hydrate Shell

Hydrate forms at the interface between the CO₂ gas and the water-saturated sediment slurry during forced gas injection experiments. The hydrate shell inherits the shape of the gas-driven fractures and maintains cavities open and interconnected even in very soft slurries (Figure 7, test 19). In our experiments, these continuous hydrate layers are approximately 120 microns across or thinner (Subramanian, 2000). The hydrate shells appear continuous and thicken by slow gas diffusion through the solidifying hydrate (note: The gas-filled cavity is the only source of gas molecules). In time, thin hydrate lenses grow into the slurry (Figure 7).

4.3. Additional Effects

4.3.1. Time

We observed long induction times and often recorded weak but long P-T hydrate formation signatures that did not render tomographic evidence of any hydrate mass; these “negative result” experiments are not included in Table 2 (note: 45% of the experiments conducted during the 3-year study produced discernible tomographic images). In other cases, CT scans confirmed that the lens geometry and the internal hydrate structure continued evolving long after the thermal spike had vanished (e.g., tests 20 and 21). Beyond stochastic nucleation, time emerges as a central variable in all cases in this study through concurrent time-dependent processes such as gas transport, sediment compressibility, rate of reaction and heat dissipation, and ripening.

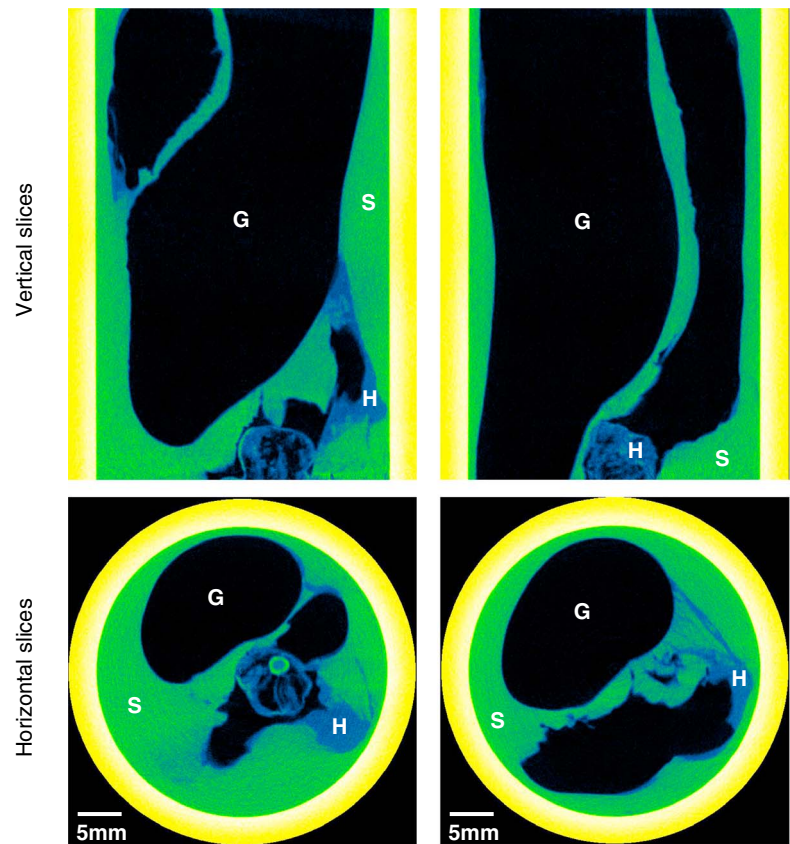
4.3.2. The Influence of Mineral Wettability

Capillary and cryogenic suction compete for water during ice-to-hydrate transformation (tests 9–12; refer to Figure 5). When the mineral surface is strongly hydrophilic, the ice lens size decreases during hydrate formation because the rate of capillary suction exceeds the rate of hydrate formation (Figure 8a; test 12); in fact, thin ice lenses vanish into the sediment before hydrate formation starts. But it is a competition not only among rates but also among magnitudes: If cryogenic suction were stronger than capillary suction, growing hydrate crystals would pull the water back out of the imbibed sediment. Clearly, these observations apply to the ice-seed method used for hydrate bearing sands: Water migrates and forms capillary menisci before hydrate formation, and the resulting pore habit is not pore-filling but cementing.

By contrast, water does not invade fumed hydrophobic silica (Figure 8b; tests 13 and 14); however, the ice/hydrate lens shape becomes more spherical during ice-to-hydrate transformation; clearly, the surface tension in liquid water manifests itself before hydrate formation (Jung & Santamarina, 2012).

4.3.3. Hydrate Dissociation

We used either depressurization or heating to cause hydrate dissociation. Hydrate dissociation by depressurization exhibits a decrease in temperature due to the endothermic transformation (Figure 3: test 11).



Labels: S=Sediment (green), G=Gas (black), H=Hydrate (blue)

Figure 7. Forced CO₂ gas invasion in kaolinite slurry (test 19 in Table 2). Multiple hydrate lenses form between the two gas bodies. A hydrate shell covers the gas-sediment interface and prevents the slurry from collapsing.

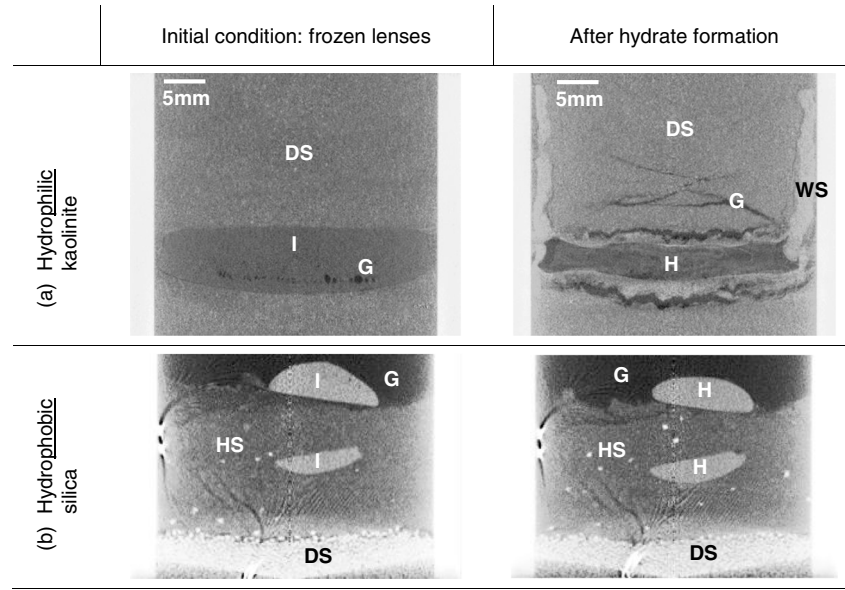
Dissociation cooling lowers the temperature below water freezing (tests 7 and 11). Conversely, dissociation by heating leads to pressure increase under isochoric conditions (Figure 3: tests 19 and 21; Kwon et al., 2008). When segregated hydrate dissociates, it leaves behind the blocky sediment structure made of overconsolidated sediments that compacted due to cryogenic suction.

5. Discussion

All the evidence suggests that the initially porous and permeable hydrate mass can sustain gas transport much faster than diffusive transport through solid hydrate. Then, hydrate accumulation continues by extracting water from the sediment and transporting gas through the porous hydrate mass. This exo-pore growth mechanism can be much faster than diffusion-limited growth. The initially porous hydrate structure gradually evolves toward a solid structure with less surface area through Ostwald ripening.

Sudden hydrate formation well inside the stability field produces a clear thermal spike; thereafter, hydrate continues to grow at a slower diffusion-limited rate and without a thermal signature. Note that thermal diffusion is orders of magnitude faster than chemical diffusion in these systems.

Gas in gas-driven fractures is consumed by hydrate formation and fractures gradually clench. The gas-filled cavity is the only source of gas molecules; therefore, the thickening of the hydrate shell at the gas-sediment interface is sustained by gas transport across the hydrate shell itself. Without an additional gas supply, the thin hydrate shells that formed on the walls of small gas driven openings may dissociate and vanish as gas molecules diffuse into the water-saturated sediment.



Labels: DS=Dry Sediment, HS=Hydrophobic Silica, WS=Wet Sediment, I=Ice, G=Gas, H=Hydrate

Figure 8. Ice-to-CO₂ hydrate transformation. (a) Large ice lens buried within dry hydrophilic kaolinite—test 12 in Table 2. There is a competition between the rate of ice-to-hydrate transformation and the rate of water imbibition into the hydrophilic clay (wet clay appears brighter); thus, this image captures the competition between capillarity and cryogenic suction (b) ice lenses on top and within dry hydrophobic silica—test 14 in Table 2. The dry hydrophobic silica is very loosely packed and it appears darker than ice and hydrate lenses.

Hydrate growth displaces mineral grains when particle-level forces induced by the growing hydrate mass exceed particle-level forces induced by the acting effective stresses (Clennell et al., 2000). The ratio between the lens thickness “*t*” and the separation between lenses “*L*” provides a first order estimate of the compressive strain the sediment experiences to make space for a hydrate lens. Invoking Terzaghi’s compressibility relation for sediments, the ratio between lens thickness and separation *t/L* is

$$\frac{t}{L} = C_c \frac{1}{1 + e_0} \log \left(\frac{\sigma'_0 + U}{\sigma'_0} \right) \quad (1)$$

where *e*₀ and σ'_0 are the initial void ratio and effective stress and *C*_{*c*} is the sediment compressibility. As per Laplace’s equation, the cryogenic suction *U* is inversely proportional to the curvature of the interface *r* (equal to the pore size if the hydrate-mineral contact angle is 180°),

$$U = 2 \frac{T_s}{r} \quad (2)$$

where *T*_{*s*} is the surface tension between water and hydrate or

$$U = 2 \frac{T_s S_s}{e_0} \quad (3)$$

if pore size is estimated in terms of the specific surface *S*_{*s*} [m⁻¹]. Then, we can conclude that lenses will be thicker and closer to each other in compressible, high specific surface sediments subjected to low effective stress. The sequence of tomographic images shown in Figure 4, and all other results in this study corroborate this deduction. As a corollary, small laboratory experiments, that is, small *L*, limit the range of sediments that can exhibit segregated hydrate.

Cryogenic suction during displacive hydrate formation extracts water from the surrounding sediment. The compacted, stiffer sediments yield faster wave speed, higher mechanical strength, and lower permeability than the original water-saturated sediment. Only partial swelling takes place during hydrate dissociation, and excess water drains out of the remnant compacted and blocky sediment structure. Consequently, gas

production in fine-grained sediments would cause volumetric contraction at least as high as the segregated hydrate volume.

6. Conclusions

Most hydrate accumulations in nature are found in fine-grained sediments. Hydrate formation in fine-grained sediments is limited by gas transport. We used different strategies to accelerate the supply of guest molecules to the hydrate formation front, to overcome the nucleation barrier, and to explore long-term diffusion controlled gas hydrate formation. This study highlights the inherent challenges in hydrate formation in fine-grained sediments within relatively short laboratory time scales. The main conclusions are as follows:

1. Hydrate formation in fine-grained sediments is inherently displacive and segregated. Hydrate formation extracts water from the sediments, the surrounding medium becomes compacted, and the effective P-T phase boundary migrates during formation. A compacted and blocky sediment structure remains upon hydrate dissociation.
2. Analytical and experimental results show that lenses are thicker and closer to each other in compressible, high specific surface sediments subjected to low effective stress.
3. Gas supply to the hydrate formation front controls the rate of hydrate formation. Exo-pore growth conveys a striped and porous structure to freshly formed hydrate. This open structure is an effective path for gas transport to the hydrate-sediment interface and can sustain hydrate growth much faster than diffusive gas transport.
4. CT scans confirm that the lens geometry and internal hydrate structure continue evolving long after the exothermal thermal spike has vanished. Beyond stochastic nucleation, time is implicit in multiple concurrent time-dependent processes, including gas, water and heat transport, sediment compressibility, and rate of reaction.
5. Ice seeding has been frequently used to expedite hydrate formation in coarse-grained sediments. We attempted this method to grow hydrate lenses at predefined locations. Results show that ice-to-hydrate transformation goes through a liquid stage at premelt temperatures; then, capillarity and cryogenic suction compete, and water gets redistributed faster than hydrate reformation.

Acknowledgments

Seth Mallett helped in the execution of various experiments conducted as part of this study. Gabrielle Abelskamp edited earlier versions of this manuscript. Support for this research was provided by the USA Department of Energy, the Goizueta Foundation, and the KAUST endowment. All the experimental data used in this article are available in Lei's PhD thesis (Lei, 2017).

References

- Aman, Z. M., Brown, E. P., Sloan, E. D., Sum, A. K., & Koh, C. A. (2011). Interfacial mechanisms governing cyclopentane clathrate hydrate adhesion/cohesion. *Physical Chemistry Chemical Physics*, 13(44), 19,796–19,806. <https://doi.org/10.1039/C1CP21907C>
- Aman, Z. M., Olcott, K., Pfeiffer, K., Sloan, E. D., Sum, A. K., & Koh, C. A. (2013). Surfactant adsorption and interfacial tension investigations on cyclopentane hydrate. *Langmuir*, 29(8), 2676–2682. <https://doi.org/10.1021/la3048714>
- Anderson, G. K. (2003). Enthalpy of dissociation and hydration number of carbon dioxide hydrate from the Clapeyron equation. *The Journal of Chemical Thermodynamics*, 35(7), 1171–1183. [https://doi.org/10.1016/S0021-9614\(03\)00093-4](https://doi.org/10.1016/S0021-9614(03)00093-4)
- Anderson, R., Llamedo, M., Tohidi, B., & Burgass, R. W. (2003). Experimental measurement of methane and carbon dioxide clathrate hydrate equilibria in mesoporous silica. *The Journal of Physical Chemistry B*, 107(15), 3507–3514. <https://doi.org/10.1021/jp0263370>
- Azmatch, T. F., Segoo, D. C., Arenson, L. U., & Biggar, K. W. (2012). New ice lens initiation condition for frost heave in fine-grained soils. *Cold Regions Science and Technology*, 82(0), 8–13. <https://doi.org/10.1016/j.coldregions.2012.05.003>
- Boswell, R. (2009). Is gas hydrate energy within reach? *Science*, 325(5943), 957–958. <https://doi.org/10.1126/science.1175074>
- Boswell, R., & Collett, T. S. (2011). Current perspectives on gas hydrate resources. *Energy & Environmental Science*, 4(4), 1206–1215. <https://doi.org/10.1039/C0EE00203H>
- Chen, F., Hu, Y., Feng, D., Zhang, X., Cheng, S., Cao, J., et al. (2016). Evidence of intense methane seepages from molybdenum enrichments in gas hydrate-bearing sediments of the northern South China Sea. *Chemical Geology*, 443, 173–181. <https://doi.org/10.1016/j.chemgeo.2016.09.029>
- Clenell, M. B., Henry, P., Hovland, M., Booth, J. S., Winters, W. J., & Thomas, M. (2000). Formation of natural gas hydrates in marine sediments: Gas hydrate growth and stability conditioned by host sediment properties. *Annals of the New York Academy of Sciences*, 912(1), 887–896. <https://doi.org/10.1111/j.1749-6632.2000.tb06842.x>
- Clenell, M. B., Hovland, M., Booth, J. S., Henry, P., & Winters, W. J. (1999). Formation of natural gas hydrates in marine sediments: 1. Conceptual model of gas hydrate growth conditioned by host sediment properties. *Journal of Geophysical Research*, 104(B10), 22,985–23,003. <https://doi.org/10.1029/1999JB900175>
- Clenell, M. B., Judd, A., & Hovland, M. (2000). Movement and accumulation of methane in marine sediments: Relation to gas hydrate systems. In *Natural Gas Hydrate in Oceanic and Permafrost Environments* (Chap. 9, pp. 105–122). Dordrecht, Netherlands: Kluwer Academic Publishers.
- Collett, T. S., Riedel, M., Cochran, J. R., Boswell, R., Kumar, P., & Sathe, A. V. (2008). Indian continental margin gas hydrate prospects: Results of the Indian National Gas Hydrate Program (NGHP) expedition 01. In *Proceedings of the 6th International Conference on Gas Hydrates* (ICGH 2008). Vancouver, British Columbia, Canada, July 6–10 2008.
- Cook, A. E., Goldberg, D., & Kleinberg, R. L. (2008). Fracture-controlled gas hydrate systems in the northern Gulf of Mexico. *Marine and Petroleum Geology*, 25(9), 932–941. <https://doi.org/10.1016/j.marpetgeo.2008.01.013>
- Dai, S., Lee, C., & Carlos Santamarina, J. (2011). Formation history and physical properties of sediments from the Mount Elbert gas hydrate stratigraphic test well, Alaska North Slope. *Marine and Petroleum Geology*, 28(2), 427–438. <https://doi.org/10.1016/j.marpetgeo.2010.03.005>

- Dai, S., Lee, J. Y., & Santamarina, J. C. (2014). Hydrate nucleation in quiescent and dynamic conditions. *Fluid Phase Equilibria*, 378(Supplement C), 107–112. <https://doi.org/10.1016/j.fluid.2014.07.006>
- Dai, S., Santamarina, J. C., Waite, W. F., & Kneafsey, T. J. (2012). Hydrate morphology: Physical properties of sands with patchy hydrate saturation. *Journal of Geophysical Research*, 117, B11205. <https://doi.org/10.1029/2012JB009667>
- Ebinuma, T., Kamata, Y., Minagawa, H., Ohmura, R., Nagao, J., & Narita, H. (2005). *Mechanical properties of sandy sediment containing methane hydrate*. Paper presented at Fifth International Conference on Gas Hydrates, Tapir Acad., Trondheim, Norway.
- Gardner, J. V., Malik, M., & Walker, S. (2009). Plume 1400 meters high discovered at the seafloor off the northern California margin. *Eos, Transactions American Geophysical Union*, 90(32), 275–275. <https://doi.org/10.1029/2009EO320003>
- Ghosh, R., Sain, K., & Ojha, M. (2010). Effective medium modeling of gas hydrate-filled fractures using the sonic log in the Krishna-Godavari basin, offshore eastern India. *Journal of Geophysical Research*, 115, B06101. <https://doi.org/10.1029/2009JB006711>
- Graves, C. A., James, R. H., Sapart, C. J., Stott, A. W., Wright, I. C., Berndt, C., et al. (2017). Methane in shallow subsurface sediments at the landward limit of the gas hydrate stability zone offshore western Svalbard. *Geochimica et Cosmochimica Acta*, 198, 419–438. <https://doi.org/10.1016/j.gca.2016.11.015>
- Handa, Y. P., & Stupin, D. Y. (1992). Thermodynamic properties and dissociation characteristics of methane and propane hydrates in 70-ÅNG-radius silica gel pores. *The Journal of Physical Chemistry*, 96(21), 8599–8603. <https://doi.org/10.1021/j100200a071>
- Hofmann, D., Preuss, G., & Mätzler, C. (2015). Evidence for biological shaping of hair ice. *Biogeosciences*, 12(14), 4261–4273. <https://doi.org/10.5194/bg-12-4261-2015>
- Jang, J., & Santamarina, J. C. (2016). Fines classification based on sensitivity to pore-fluid chemistry. *Journal of Geotechnical and Geoenvironmental Engineering*, 142(4), 06015018. [https://doi.org/10.1061/\(ASCE\)GT.1943-5606.0001420](https://doi.org/10.1061/(ASCE)GT.1943-5606.0001420)
- Jin, Y., Nagao, J., Hayashi, J., Shimada, W., Ebinuma, T., & Narita, H. (2008). Observation of Xe hydrate growth at gas-ice interface by microfocus X-ray computed tomography. *The Journal of Physical Chemistry C*, 112(44), 17253–17256. <https://doi.org/10.1021/jp803525m>
- Jung, J. W., Espinoza, D. N., & Santamarina, J. C. (2010). Properties and phenomena relevant to CH₄-CO₂ replacement in hydrate-bearing sediments. *Journal of Geophysical Research*, 115, B10102. <https://doi.org/10.1029/2009JB000812>
- Jung, J. W., & Santamarina, J. C. (2012). Hydrate formation and growth in pores. *Journal of Crystal Growth*, 345(1), 61–68. <https://doi.org/10.1016/j.jcrysgro.2012.01.056>
- Katsuki, D., Ohmura, R., Ebinuma, T., & Narita, H. (2006). Formation, growth and ageing of clathrate hydrate crystals in a porous medium. *Philosophical Magazine*, 86(12), 1753–1761. <https://doi.org/10.1080/14786430500509062>
- Kwon, T.-H., Cho, G.-C., & Santamarina, J. C. (2008). Gas hydrate dissociation in sediments: Pressure-temperature evolution. *Geochemistry, Geophysics, Geosystems*, 9, Q03019. <https://doi.org/10.1029/2007GC001920>
- Lee, J. Y., Jung, J. W., Lee, M. H., Bahk, J. J., Choi, J., Ryu, B. J., & Schultheiss, P. C. (2013). Pressure core based study of gas hydrates in the Ullung Basin and implication for geomechanical controls on gas hydrate occurrence. *Marine and Petroleum Geology*, 47(0), 85–98. <https://doi.org/10.1016/j.marpetgeo.2013.05.021>
- Lee, J. Y., Yun, T. S., Santamarina, J. C., & Ruppel, C. (2007). Observations related to tetrahydrofuran and methane hydrates for laboratory studies of hydrate-bearing sediments. *Geochemistry, Geophysics, Geosystems*, 8, Q06003. <https://doi.org/10.1029/2006GC001531>
- Lei, L. (2017). *Gas hydrate in fine-grained sediments—Laboratory studies and coupled processes analyses*. Atlanta: Georgia Institute of Technology.
- Li, Y., & Somorjai, G. A. (2007). Surface premelting of ice. *The Journal of Physical Chemistry C*, 111(27), 9631–9637. <https://doi.org/10.1021/jp071102f>
- Makogon, Y. F. (1997). *Hydrates of hydrocarbons*. Tulsa, OK: PennWell Books, PennWell Publishing Company.
- Miller, R. D. (1972). Freezing and heaving of saturated and unsaturated soils. In *51st Annual Meeting of the Highway Research Board*. Washington District of Columbia, United States.
- Moridis, G. J., Collett, T. S., Boswell, R., Kurihara, M., Reagan, M. T., Koh, C., & Sloan, E. D. (2009). Toward production from gas hydrates: Current status, assessment of resources, and simulation-based evaluation of technology and potential. *SPE Reservoir Evaluation & Engineering*, 12(05), 745–771. <https://doi.org/10.2118/114163-PA>
- O'Neill, K., & Miller, R. D. (1985). Exploration of a rigid ice model of frost heave. *Water Resources Research*, 21(3), 281–296. <https://doi.org/10.1029/WR021i003p00281>
- Palomino, A. M., & Santamarina, J. C. (2005). Fabric map for kaolinite: Effects of pH and ionic concentration on behavior. *Clays and Clay Minerals*, 53(3), 211–223. <https://doi.org/10.1346/CCMN.2005.0530302>
- Park, T., Kim, H.-S., & Kwon, T.-H. (2016). *A small pore size effect on dissociation behavior of gas hydrates in fine-grained sediments*. Paper presented at Energy Geotechnics: Proceedings of the 1st International Conference on Energy Geotechnics, ICEGT 2016, Kiel, Germany, 29–31 August 2016, CRC Press.
- Plaschke, M., Schäfer, T., Bundschuh, T., Ngo Manh, T., Knopp, R., Geckeis, H., & Kim, J. (2001). Size characterization of bentonite colloids by different methods. *Analytical Chemistry*, 73(17), 4338–4347. <https://doi.org/10.1021/ac010116t>
- Rees, E. V. L., Priest, J. A., & Clayton, C. R. I. (2011). The structure of methane gas hydrate bearing sediments from the Krishna-Godavari Basin as seen from micro-CT scanning. *Marine and Petroleum Geology*, 28(7), 1283–1293. <https://doi.org/10.1016/j.marpetgeo.2011.03.015>
- Rempel, A. (2011a). A model for the diffusive growth of hydrate saturation anomalies in layered sediments. *Journal of Geophysical Research*, 116, B10105. <https://doi.org/10.1029/2011JB008484>
- Rempel, A. W. (2011b). Microscopic and environmental controls on the spacing and thickness of segregated ice lenses. *Quaternary Research*, 75(02), 316–324. <https://doi.org/10.1016/j.yqres.2010.07.005>
- Schwalenberg, K., Rippe, D., Koch, S., & Scholl, C. (2017). Marine-controlled source electromagnetic study of methane seeps and gas hydrates at Opouawe Bank, Hikurangi margin, New Zealand. *Journal of Geophysical Research: Solid Earth*, 122, 3334–3350. <https://doi.org/10.1002/2016JB013702>
- Seshadri, K., Wilder, J. W., & Smith, D. H. (2001). Measurements of equilibrium pressures and temperatures for propane hydrate in silica gels with different pore-size distributions. *The Journal of Physical Chemistry B*, 105(13), 2627–2631. <https://doi.org/10.1021/jp0040244>
- Subramanian, S. (2000). *Measurement of clathrate hydrates containing methane and ethane using Raman spectroscopy*. Golden, CO: Colorado School of Mines.
- Ta, X. H., Yun, T. S., Muhunthan, B., & Kwon, T. H. (2015). Observations of pore-scale growth patterns of carbon dioxide hydrate using X-ray computed microtomography. *Geochemistry, Geophysics, Geosystems*, 16(3), 912–924. <https://doi.org/10.1002/2014GC005675>
- Taber, S. (1930). The mechanics of frost heaving. *The Journal of Geology*, 38(4), 303–317. <https://doi.org/10.1086/623720>
- Tohidi, B., Anderson, R., Clennell, M. B., Burgass, R. W., & Biderkab, A. B. (2001). Visual observation of gas-hydrate formation and dissociation in synthetic porous media by means of glass micromodels. *Geology*, 29(9), 867–870. [https://doi.org/10.1130/0091-7613\(2001\)029%3C0867:vooghf%3E2.0.co;2](https://doi.org/10.1130/0091-7613(2001)029%3C0867:vooghf%3E2.0.co;2)

- Uchida, T., Ebinuma, T., Takeya, S., Nagao, J., & Narita, H. (2001). Effects of pore sizes on dissociation temperatures and pressures of methane, carbon dioxide, and propane hydrates in porous media. *The Journal of Physical Chemistry B*, *106*(4), 820–826. <https://doi.org/10.1021/jp012823w>
- Viggiani, G., Andò, E., Takano, D., & Santamarina, J. (2015). Laboratory X-ray tomography: A valuable experimental tool for revealing processes in soils. *Geotechnical Testing Journal*, *38*(1), 61–71. <https://doi.org/10.1520/GTJ20140060>
- Waite, W. F., Santamarina, J. C., Cortes, D. D., Dugan, B., Espinoza, D. N., Germaine, J., et al. (2009). Physical properties of hydrate-bearing sediments. *Reviews of Geophysics*, *47*, RG4003. <https://doi.org/10.1029/2008RG000279>
- Yamamoto, K., & Dallimore, S. (2008). Aurora-JOMEC-NRCan Mallik 2006–2008 gas hydrate research project progress. *Fire in the Ice*, *8*(3), 1–5.
- Yamamoto, K., Inada, N., Kubo, S., Fujii, T., & Suzuki, K. (2012). Pressure core sampling in the eastern Nankai trough. *Fire in the Ice*, *12*(2), 1–6.
- Yun, T. S., Lee, C., Lee, J.-S., Bahk, J. J., & Santamarina, J. C. (2011). A pressure core based characterization of hydrate-bearing sediments in the Ulleung Basin, Sea of Japan (East Sea). *Journal of Geophysical Research*, *116*, B02204. <https://doi.org/10.1029/2010JB007468>
- Yun, T. S., Santamarina, J. C., & Ruppel, C. (2007). Mechanical properties of sand, silt, and clay containing tetrahydrofuran hydrate. *Journal of Geophysical Research*, *112*, B04106. <https://doi.org/10.1029/2006JB004484>
- Zatsepina, O. Y., & Buffett, B. (2001). Experimental study of the stability of CO₂-hydrate in a porous medium. *Fluid Phase Equilibria*, *192*(1-2), 85–102. [https://doi.org/10.1016/S0378-3812\(01\)00636-7](https://doi.org/10.1016/S0378-3812(01)00636-7)
- Zhong, Y., & Rogers, R. E. (2000). Surfactant effects on gas hydrate formation. *Chemical Engineering Science*, *55*(19), 4175–4187. [https://doi.org/10.1016/S0009-2509\(00\)00072-5](https://doi.org/10.1016/S0009-2509(00)00072-5)